Acta Materialia 132 (2017) 479–490

Contents lists available at ScienceDirect

Acta Materialia

journal homepage: www.elsevier.com/locate/actamat

Full length article

Microstructural damage of α-Al_2O_3 by high energy density plasma

Q. Yang [a], K. Kalathiparambil [b], D.T. Elg [b], D. Ruzic [b], W.M. Kriven [a, *]

[a] Department of Materials Science and Engineering, University of Illinois at Urbana-Champaign, Illinois 61801, USA
[b] Center for Plasma-Material Interaction, Department of Nuclear, Plasma, and Radiological Engineering, University of Illinois at Urbana-Champaign, Illinois 61801, USA

ARTICLE INFO

Article history:
Received 23 December 2016
Received in revised form
17 April 2017
Accepted 25 April 2017
Available online 28 April 2017

Keywords:
Plasma
Alumina
Aluminum
Transmission electron microscopy

ABSTRACT

One limitation on plasma thruster lifetime for space propulsion is plasma erosion of ceramic insulators. The underlying plasma erosion mechanism remains scarcely understood. In this work, polycrystalline α-Al_2O_3 was exposed to a high energy density plasma for up to 30 min using Cu and W electrodes. The damaged structures were studied by scanning and transmission electron microscopies. It was found that plasma-induced damage includes not only surface erosion but also damage down to a depth of ~1 μm. The surface damage including cracking, formation of surface nanostructures, γ-Al_2O_3 and epitaxial intergrowths of α-Al_2O_3, is caused mainly by ion-based sputtering, rapid surface melting and quenching. Deeper damage, i.e. formation of Al nanoparticles and O_2 bubbles, is caused by the electron-induced decomposition of both α- and γ-Al_2O_3 via electronic excitation. Electrode impurities, especially the W impurities sunken in the molten Al_2O_3, act as a local heat source and cause expansion of γ-Al_2O_3 and Al regions. Furthermore, the impurities react with Al to form Al_2Cu and Al_5(W,Cu) particles. The Al_2Cu are formed as surface dendrites and nanoparticles within the Al matrix. The Al_5(W,Cu) having Al- and W-rich nano domains is determined to be a rhombohedral structure with lattice parameters of $a = 0.490(3)$ nm, $c = 2.632(4)$ nm and a space group of $R\bar{3}c$. This study indicates that besides surface erosion, deeper damage caused by electrons and impurities should be considered when evaluating thruster plasma damage on ceramics.

1. Introduction

With the development of plasma for fusion reactors and space propulsion, plasma-material interactions are of great importance as they critically influence the safety and performance of fusion reactors and plasma thrusters [1]. Until now, plasma-material interaction studies have been made mainly on tungsten (W) used in fusion reactors [2], while those for plasma thrusters are far from being sufficient [3,4]. Unlike fusion reactors, plasma thrusters require the use of ceramic insulators as a discharge chamber, thruster wall and nozzle [5–8]. These ceramics have high survivability under high temperatures, an insulating nature, low sputtering yield, and a low effect of their sputtering products on spacecraft surface optical and thermal properties [5,7]. Candidate ceramics are BN and its composites, SiO_2, and Al_2O_3 [8].

The high density and high temperature thruster plasma conditions (T_e ~ 2–40 eV, n_e ~ 10^{17} - 10^{20} m^{-3}) can cause excess erosion of ceramics. Such erosion results in mass loss, change of plasma equilibrium boundary conditions and eventually thruster failure because of deficient thermal and electrical insulation [5]. To date, studies on plasma erosion have been investigated in terms of erosion rate [9,10], surface morphology and chemical composition change [3,4,11]. These erosions are explained by ion-induced surface sputtering and implantation based on elastic collisions. However, for plasma composed of multiple species, besides elastic collision, one damage mechanism should be considered is ionization, especially for ceramics with covalent or ionic bonds. By damaging the electronic structure, ionization can cause bond rupture, charged defects, enhanced defect diffusion, electronic excitation, and even permanent defects [12,13]. This damage can be caused by ions, electrons and even photons, and is accelerated at elevated temperatures [14]. For the thruster plasma with relatively low ion energy (keV or lower) but high density electrons, photons and accompanied high temperature, it is possible that plasma damage on ceramics can occur via multiple mechanisms rather than surface sputtering. Comprehensive understanding of plasma erosion behavior on ceramics is crucial.

* Corresponding author.
E-mail address: kriven@illinois.edu (W.M. Kriven).

http://dx.doi.org/10.1016/j.actamat.2017.04.058
1359-6454/

In addition to plasma, inevitable electrode impurities caused by plasma erosion can also be injected into ceramics, adding complexity to the measurement of sputtering yield as well as erosion kinetics. This complexity becomes evident during prolonged operation at increased impurity fluence. Currently, materials used for plasma electrodes are copper, brass, molybdenum, aluminum, stainless steel and copper-tungsten alloy. Among them, copper (Cu) and copper-tungsten (Cu-W) alloys with low erosion rates are preferred [15].

In this study, Al_2O_3 was exposed to a z-pinch plasma using Cu and W electrodes. The z-pinch plasma offers a short duration (~10–50 ns) but high energy density (n_e ~ 10^{19} - 10^{20} cm^{-3}) plasma, causing high temperature and extremely high heating and cooling rates. Such a z-pinch plasma is normally used for extreme ultraviolet (EUV) lithography [16], thin film deposition [17] and surface nanotechnology [18,19]. Because of the equivalent plasma condition to the thruster plasma, but possessing a much higher electron density, the z-pinch plasma can be used to study thruster plasma damage of ceramics after prolonged operation. By studying the damaged microstructure under different plasma exposure times using scanning and transmission electron microscopy (SEM, TEM), we aim to acquire a comprehensive understanding of the effects of plasma and electron impurity damage on Al_2O_3 ceramic.

2. Experimental

Polycrystalline α-Al_2O_3 was sintered at 1600 °C for 2 h with a ramping rate of 7 °C/min, by using commercially available alumina A16SG powders (Sigma-Aldrich, St Louis, MO) with a chemical purity of 99.8%. The sintered pellets were 10 mm in diameter and 3 mm in thickness. The relative pellet density was of >98.0%, and the average grain size was ~3 μm. The pellets were sliced in half from the middle thickness plane. The sliced plane was then ground down to a thickness of 1 mm and mirror-polished down with a grit of 0.25 μm diamond paste. After annealing for 30 min at 1300 °C in air to remove surface residual damage and carbon contamination, samples were exposed to plasma.

The plasma experiment was performed in the XCEED facility (developed in the Center for Plasma-Material Interaction (CPMI) at the University of Illinois at Urbana-Champaign), which could produce an energetic, high density (T_e ~ 30 eV, n_e ~ 10^{20} cm^{-3}, ionization states up to +12) z-pinch plasma. Each pulse lasted 10 ns, but generated an energy density of ~20 J/cm^2 [18]. A coaxial plasma gun composed of an inner W cathode and an outer Cu anode was used, where the plasma had a cylindrical dimension of 3 mm length by 1 mm radius. Ar was used as the plasma gas. At ambient temperature under a vacuum of 8 × 10^{-4} Pa, samples were positioned at 2 cm away from the pinch, and exposed at a frequency of 40 Hz and a discharge voltage of 2 kV. The exposure times ranged from 1 to 30 min. The ion energy, according to our previous measurements, could reach 14 keV with an energy distribution peak at 2.5 keV [20].

Microstructure characterizations were conducted using X-ray diffraction (XRD), SEM and TEM. XRD was carried out with Seimens-Bruker D5000 X-ray diffractometer with Cu K_α radiation (λ = 1.540598 Å). SEM was conducted with a Hitachi S4800 FE-SEM, and JEOL 6060LV SEM equipped with energy-dispersive X-ray spectroscopy (EDS). SEM acceleration voltages were set at 5 kV for imaging and 20 kV for EDS analysis, respectively. Cross-sectional TEM samples were prepared using FEI Helios 600i focused ion beam/scanning electron microscopy (FIB/SEM). During TEM sample preparation, the samples were first coated with carbon, and then a Pt/C protective layer with e- and i-beams. TEM characterization was conducted using JEOL 2010 LaB_6, JEOL 2010F scanning TEM (STEM) and JEOL 2200FS Cs-corrected STEM equipped with a high angle annular dark field (HAADF) detector, where all were performed at a voltage of 200 kV. TEM-EDS were conducted on both JEOL 2010F and JEOL 2200FS TEMs. Samples for TEM-EDS observation were welded on to Mo FIB grids.

3. Results

For the pristine α-Al_2O_3, the XRD result in Fig. 1(a) shows single phase α-Al_2O_3. TEM image in Fig. 1(b) indicates a dense and defect-free α-Al_2O_3 structure. Fig. 1(c) is a SEM image of the polished and annealed surface before plasma exposure, revealing a flat and featureless morphology. Samples after plasma exposure were observed on both surface and cross-section, as will be described below.

3.1. Surface observation

Fig. 2 presents SEM images of the Al_2O_3 samples exposed to plasma for different times. Dense spherical particles were observed on the surfaces of samples exposed for 1 and 2 min, and the average particle size increased with time up to ~500 nm (Fig. 2(a) and (b)). These particles were identified to be mainly W by EDS in Fig. 2(g), suggesting substantial sputtering of the W electrode. The aggregated particles tended to sink into the Al_2O_3 matrix (as indicated by arrows in Fig. 2(b)), causing extrusion of the surrounding matrix. Cracks having a width of ~40 nm were formed, mainly from the plasma-induced large thermal stresses. W particles were also observed to distribute and sink along the cracks. No evident surface roughening was observed in samples exposed for up to 2 min.

After plasma exposure for 3 min, as seen in Fig. 2(c), the W particle size increased up to 3 μm, but their volume fraction decreased. Crack networks were well developed with the colony size close to the grain size, indicating cracking along grain boundaries. Large amounts of spherical holes with sizes equivalent to those of the particles were distributed mainly along the cracks. These holes would be from sputtering-induced particle detachment. In addition, dark regions appeared mainly along the cracks in the form of both fine strips (~100 nm in width) and irregular shapes with sizes ranging from 1 to 20 μm. Surface features of the sample after plasma exposure for 30 min were similar to those exposed for 3 min, but extensive interlinking and expansion of the dark regions with particle clusters distributed on their surface (Fig. 2(d)). Formation of the dark regions generated surface roughening, as evidenced by tilting the sample to 52° on the specimen stage (Fig. 2(e) and (f)). These dark regions were determined to be Al by EDS shown in Fig. 2(h). Particles formed on top of the Al region contained not only W but also substantial amounts of Al (Fig. 2(i)), indicating a reaction between Al and W particles.

Besides forming along cracks, the dark Al regions also formed underneath the surface and caused surface extrusion and bursting, as shown in Fig. 3(a) and (b). Cross-sectional images in Fig. 3(c) and (d) revealed that the Al regions could extend down to a depth of ~5 μm, with particles of size >0.2 μm always embedded. Weak attachment between Al and Al_2O_3 was evidenced by the collapse of the extruded skin and micro-cavities at the Al/Al_2O_3 interface (as indicated by arrows in Fig. 3(d)).

Plasma-induced surface nanostructures were also investigated. Due to the dense impurity particles, nanostructures on the surface of Al_2O_3 were hardly distinguishable at an exposure of less than 2 min. At above 3 min exposure, spherical nanostructures with a diameter of ~20 nm were distributed uniformly on the surface of Al_2O_3, as shown in Fig. 4(a). Surface structure on the Al region was different. Nanostructures with a diameter of ~50 nm and dendrites with sizes ranging from 0.2 to 1.2 μm were observed on the surface of the Al region, as seen in Fig. 4(b) and (c), respectively. The

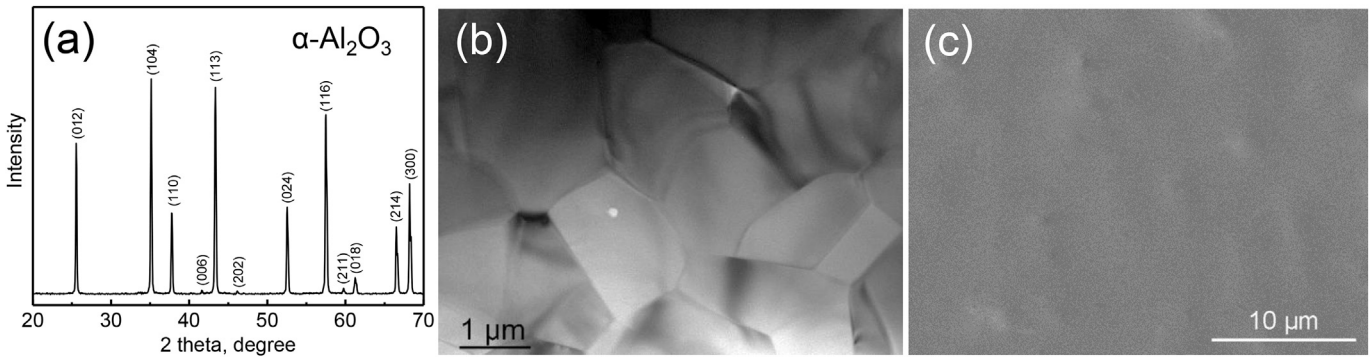

Fig. 1. Microstructure of the pristine α-Al_2O_3: (a) XRD, (b) TEM image, (c) SEM image of the polished and annealed surface before plasma exposure.

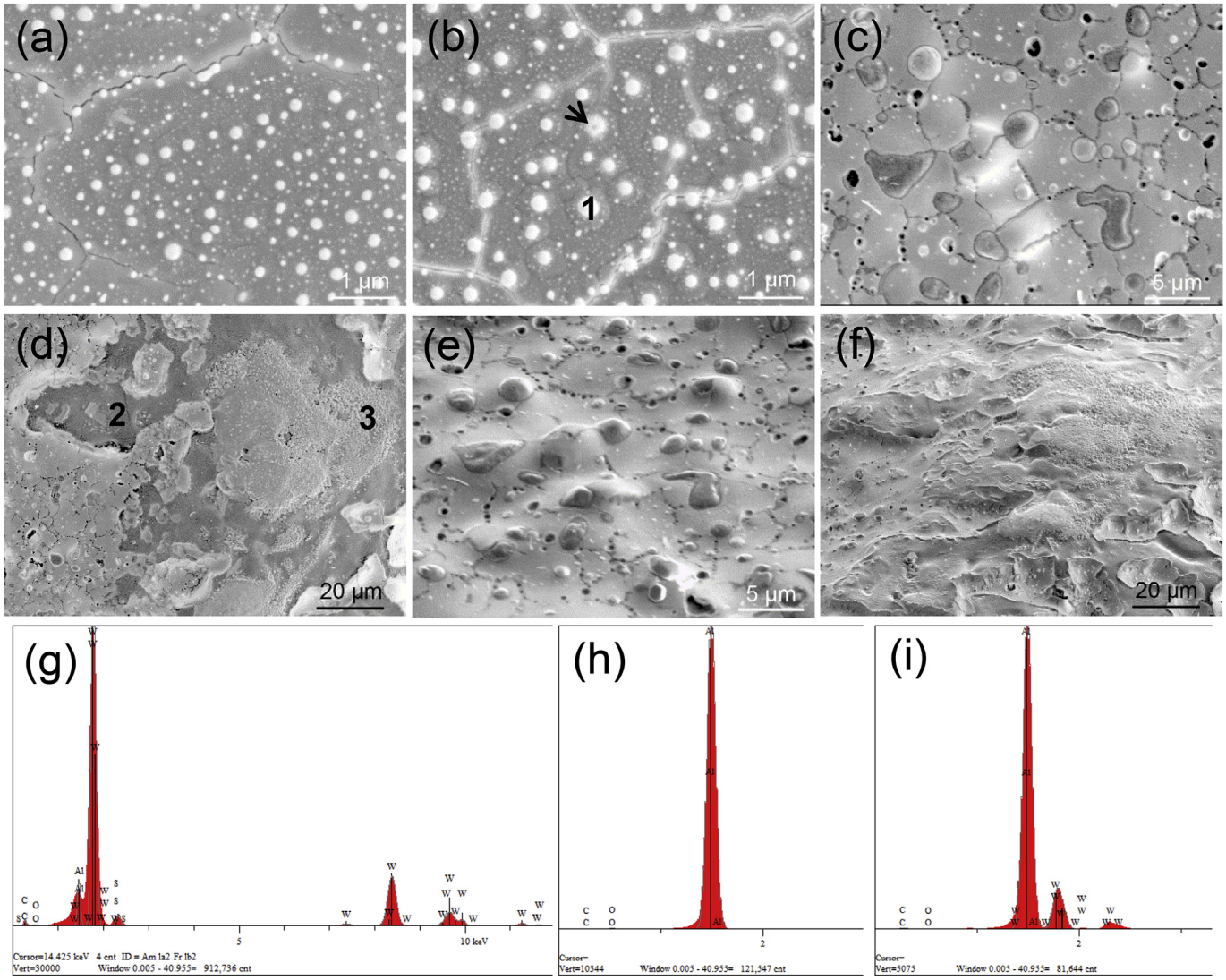

Fig. 2. SEM surface images of Al_2O_3 after plasma exposure for different time: (a) 1 min, (b) 2 min, (c) 3 min, (d) 30 min, (e) and (f) surface tilted by 52° of (c) and (d), respectively; (g)–(h) EDS spectra of regions 1, 2 and 3 marked in (b) and (d), corresponding to the particles, dark region and particles on the surface of dark region, respectively.

formation of dendrites indicated melting and solidification in the Al region. In contrast to the spherical W particles formed on the surface of Al_2O_3, surface particle clusters on the Al regions were generally faceted having size of ~1 μm, and some particles even grew into acicular shapes, as shown in Fig. 4(d).

3.2. Cross-sectional observation

Cross-sectional TEM was conducted on samples exposed for 2, 3 and 30 min, which corresponded to the microstructure before and after evident formation of Al, respectively.

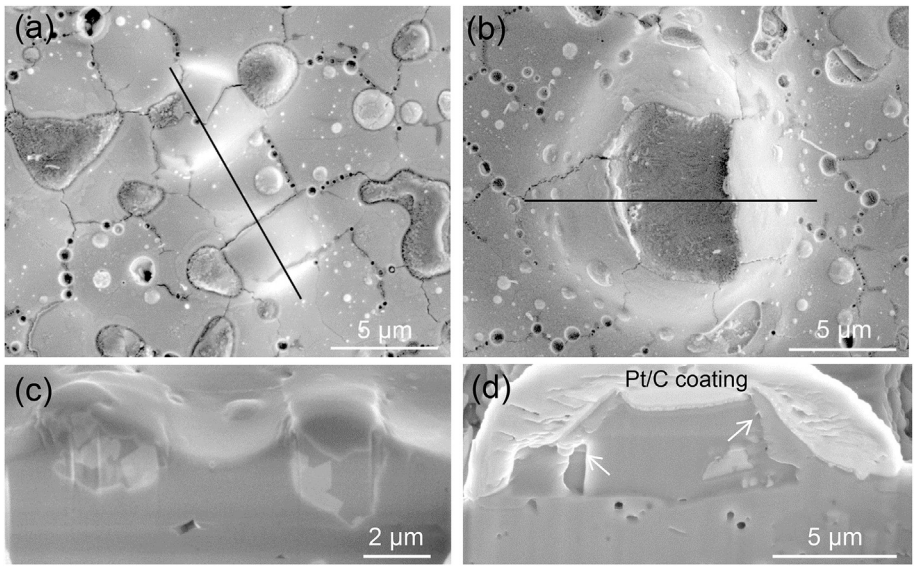

Fig. 3. Surface Al bulges on Al_2O_3 exposed to plasma for 3 min: (a) and (b) 0° tilt, (c) and (d) 52° tilt of the cross-section from lines in (a) and (b), respectively. White arrows in (d) indicate the cavities at the Al/Al_2O_3 interface.

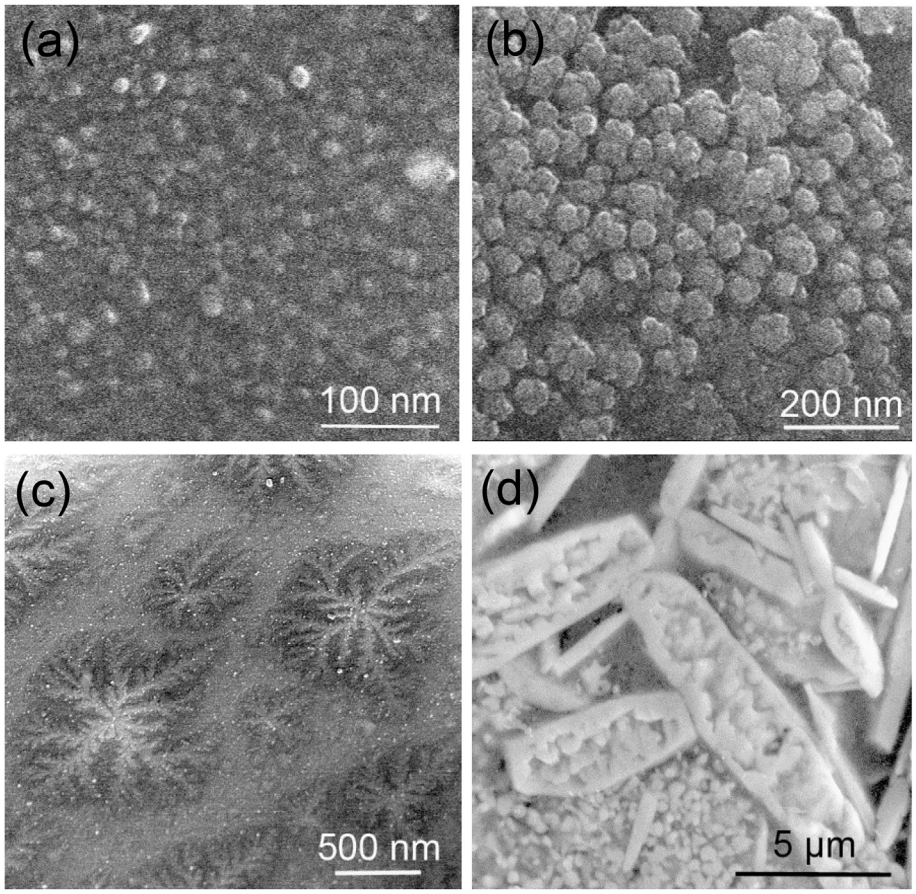

Fig. 4. Surface features after plasma exposure for 3 min: (a) nanostructures on Al_2O_3; (b) nanostructures, (c) dendrites and (d) particle clusters developed on Al after 30 min exposure.

In the sample exposed for 2 min, as seen in Fig. 5(a), dense cavities of ~2 nm in size were formed homogeneously, the cavity distribution could extent down to a depth of ~1 μm. In addition, banded regions with varied contrasts were formed along $[0001]_{\alpha\text{-}Al2O3}$ direction and extended to a depth of ~50 nm. Nano beam diffraction (NBD) patterns shown in Fig. 5(b) obtained from these regions indicated that they were crystalline α-Al_2O_3, with orientations all close to that of the substrate. The contrast difference

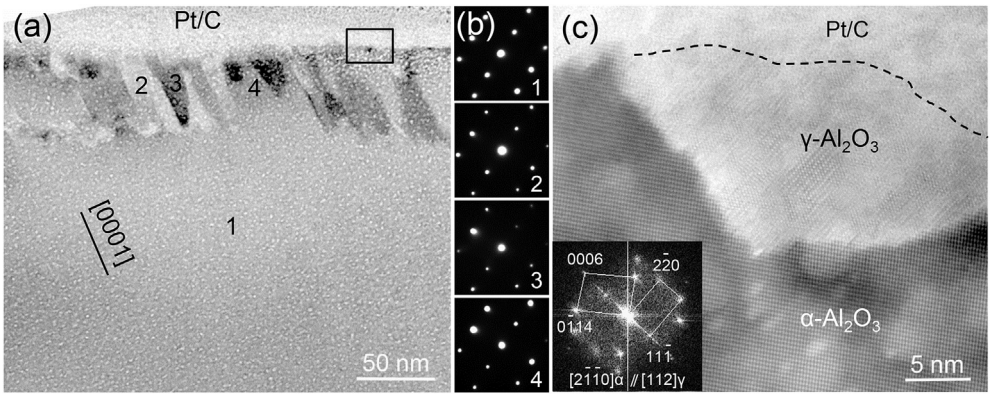

Fig. 5. Cross-sectional TEM images of α-Al_2O_3 exposed to plasma for 2 min: (a) under-focused image of the surface region, (b) NBD patterns of regions 1-4 marked in (a), (c) HRTEM image of the rectangular region marked in (a).

between adjacent bands was caused by their slight misorientations. High resolution TEM (HRTEM) observation revealed that γ-Al_2O_3 having a thickness up to 15 nm was occasionally formed on top of the α-Al_2O_3 bands, as seen in Fig. 5(c). Cavities were also formed in γ-Al_2O_3, but neither interfacial dislocations nor twins were observed. Based on the inserted fast-Fourier transformation (FFT) patterns, an orientation relationship between the γ-Al_2O_3 and α-Al_2O_3 was determined to be $(111)_\gamma//(0001)_\alpha$ and $[112]_\gamma//[1\bar{1}\bar{2}0]_\alpha$, consistent with literature [21].

Fig. 6(a) shows the microstructure near the particles in the 2 min exposed sample. Banded α-Al_2O_3 regions were still observed, while the surface γ-Al_2O_3 region around the particles was expanded into a triangular shape, with the depth increasing with decreasing distance to the particles. The larger the particle size, the further the particle sank, and the larger the region of γ-Al_2O_3 developed around it. Sinking of large particles generated large local strains as confirmed by extended deformation of the underlying α-Al_2O_3. Particle aggregation was evidenced by regions of different contrasts and cavities within a large particle. No irradiation-induced cavities were formed in the particles. Selected area electron diffraction (SAED) patterns in Fig. 6(b) confirmed the particles to be W. Reaction between the W particles and Al_2O_3 was hardly observed, as typically seen in Fig. 6(c). Although point EDS spectra of the 2 min sample did not reveal any peak from Cu, EDS mapping did show trace amount of Cu distributed only within the W particles (Fig. 6(d)-(g)).

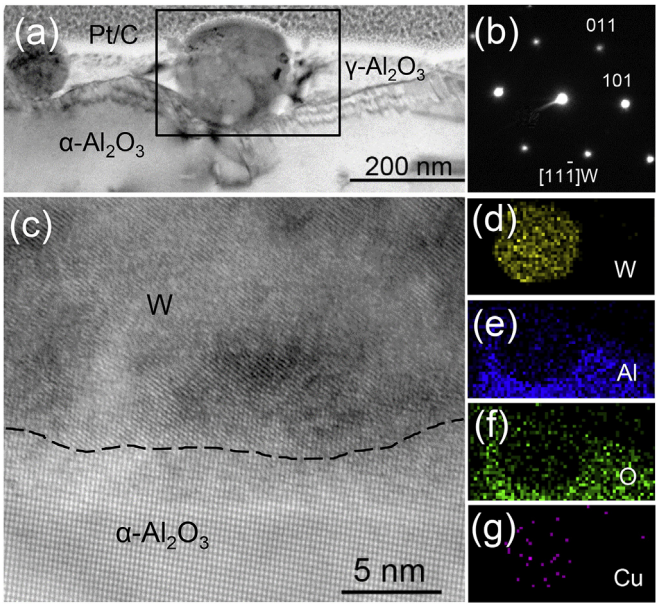

Fig. 6. Cross-sectional TEM images of W particles in Al_2O_3 sample exposed to plasma for 2 min: (a) BF-TEM image, (b) SAED patterns of W particles, (c) HRTEM image of the particle/Al_2O_3 interface, (d)–(g) EDS mappings of the rectangular region marked in (a).

TEM observation of samples after plasma exposure for 3 and 30 min revealed similar microstructural features. In particular, the sunken W particles were all reacted with Al, and were the same as the surface Al-W particles in the 30 min exposed sample in both composition and crystal structure, as will be presented later.

Fig. 7 shows typical microstructures after plasma exposure for 3 min. Fig. 7(a) and (b) highlight the Al regions developed both at the grain boundaries and from extrusion and bursting, respectively. Typical SAED patterns inserted in Fig. 7(b) revealed that each Al region was a well-developed single crystal, with $\langle 001\rangle_{Al}$ parallel to the surface normal, coincident with the general growth direction for a fcc crystal from the melt. Besides the large sunken Al-W particles, nanoparticles having sizes ranging from ~20 to ~100 nm were observed within the Al region. Interlinking and expansion of Al regions could be evidenced by the irregular-shaped Al regions and remnant Al_2O_3 colonies within the Al region, as indicated by white arrows in Fig. 7(a) and (b). The Al regions developed at the grain boundaries were surrounded by α-Al_2O_3. The bursting Al regions were always surrounded by largely expanded γ-Al_2O_3 regions that should have originally developed near the sunken W particles and grew thicker and wider with increasing exposure time. Bursting of the Al region caused deformation of the surrounding γ-Al_2O_3, as evidenced by the enlarged different contrasts in γ-Al_2O_3 and various orientations in the inserted SAED patterns in Fig. 7(c).

While there were no cavities within Al and particles, cavities were evident in both α- and γ-Al_2O_3. The cavities were distributed down to a depth of ~1 μm, similar to that in the 2 min exposed sample. Evident cavity coarsening up to ~90 nm in size was observed after 3 min plasma exposure, with the largest cavities located at the depth between ~200 and ~600 nm. Dislocations were formed and extended beneath the cavities (Fig. 7(a)). Large cavities with sizes up to 200 nm were observed at Al/Al_2O_3 and Al-W particle/Al_2O_3 interfaces. As shown in Fig. 7(d), similar to the 2 min exposed sample, surface α-Al_2O_3 bands with slight misorientations with the substrate were still formed along $[0001]_{\alpha\text{-}Al2O3}$ direction, as evidenced by the inserted NBD patterns. Besides, γ-Al_2O_3 layer was always detected on top of the α-Al_2O_3 bands, and retained the same orientation relationship with α-Al_2O_3 bands as those developed in 2 min exposed sample (Related SAED patterns were not

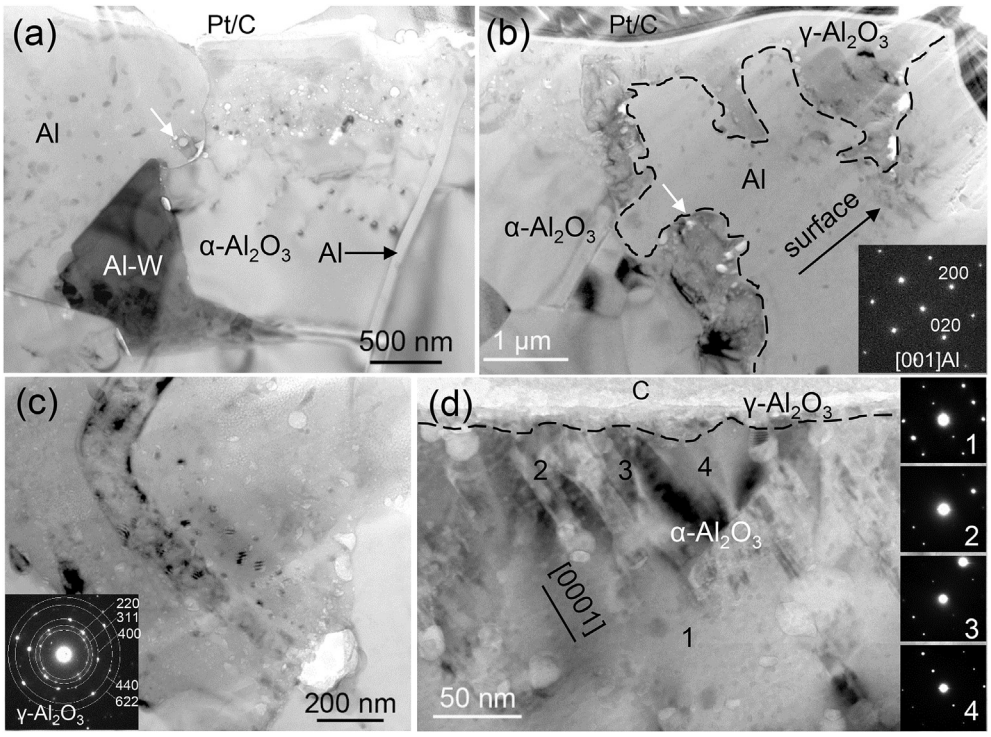

Fig. 7. Cross-sectional TEM images of Al_2O_3 sample exposed to plasma for 3 min: under-focused image of the Al regions developed both at the grain boundaries (a) and from extrusion (b), (c) deformed γ-Al_2O_3 near Al region in (b), (d) surface γ-Al_2O_3 and banded regions near the surface of α-Al_2O_3, the inserted NBD patterns correspond to regions 1–4, respectively. White arrows in (a) and (b) indicate remnant Al_2O_3 colonies within the Al region. The dotted line in (b) and (d) indicates the Al/Al_2O_3 and γ-Al_2O_3/α-Al_2O_3 interfaces, respectively.

shown). For the α-Al_2O_3 surface with no detectable particle sinking or particle sinking induced expanded γ-Al_2O_3 region, thin γ-Al_2O_3 layer was generally developed. Thickness of such γ-Al_2O_3 layer gradually increased with plasma exposure time, from ~5 nm at 2 min to ~33 nm at 30 min, as shown in Fig. 8.

The surface nanostructures exemplified in Fig. 4(a) could hardly be distinguished by TEM, either because they were too thin or amorphous with no contrast difference from the carbon coating.

It is interesting that most of the observed cavities in both α- and γ-Al_2O_3 were irregular in shape, and associated with dark features. These dark features were further determined to be irregularly-shaped nano particles in Fig. 9(a), as the Moiré fringes within them were indicative of their overlapping with Al_2O_3. All these nano particles were associated with cavities. EDS analysis of the

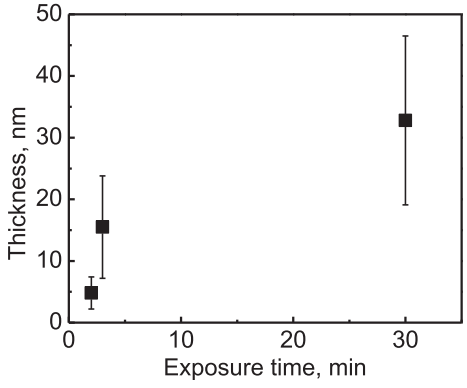

Fig. 8. Thickness evolution of γ-Al_2O_3 developed on the surface of α-Al_2O_3 with plasma exposure time.

Al_2O_3 matrix and the nano particles in Fig. 9(b) and (c) found that, comparing with the Al_2O_3, the oxygen peak in the nanoparticles almost disappeared. Fig. 9(d) and (e) show the SAED patterns of α- and γ-Al_2O_3 containing nano particles, respectively. Weak superimposed patterns from Al were distinguished from the α-Al_2O_3, as schematically shown in Fig. 9(f). The other diffraction spots originated from double diffraction as evidenced by sample tilting. In the diffraction patterns from γ-Al_2O_3, the {444} and {422} spots were elliptical rather than spherical (as indicated by arrows in Fig. 9(e)), suggesting a lattice superimposition. Because both γ-Al_2O_3 and Al are of fcc structure, and the lattice parameter of γ-Al_2O_3 is nearly 2 times that of Al, the superimposed patterns should result from Al, as schematically indicated by the circled diffraction spots in Fig. 9(g). Orientation relationships between Al and Al_2O_3 were identified as $(111)_{Al}//(0001)_{\alpha\text{-}Al2O3}$, $[011]_{Al}//[10\bar{1}0]_{\alpha\text{-}Al2O3}$, and $(200)_{Al}//(400)_{\gamma\text{-}Al2O3}$, $[011]_{Al}//[011]_{\gamma\text{-}Al2O3}$. Combining the EDS and SAED results, the dark features were identified to be Al nano particles.

Fig. 10(a) shows HAADF-STEM image of the interface between the well-developed Al region and Al_2O_3. The Al-W particles and nano particles distributed within Al region were also included with bright contrast. EDS mappings in Fig. 10(b)-(e) reveal that the Al-W particles were also enriched with Cu, and the nanoparticles were enriched only with Cu. EDS spectra in Fig. 10(f) and (g) identified the Al-W-Cu and Al-Cu nanoparticles to have compositions close to Al_5(W,Cu) and Al_2Cu, respectively.

Cross-sectional surface nanostructures and dendrites in Al regions are shown in Fig. 11(a) and (b), respectively. EDS in Fig. 11(c) identified the nanostructures to be Al_2O_3. EDS identified the surface dendrites to be Al-Cu compounds with a composition close to Al_2Cu, similar to the Al-Cu nanoparticles within Al matrix.

For the Al-Cu dendrites and nanoparticles, NBD patterns in

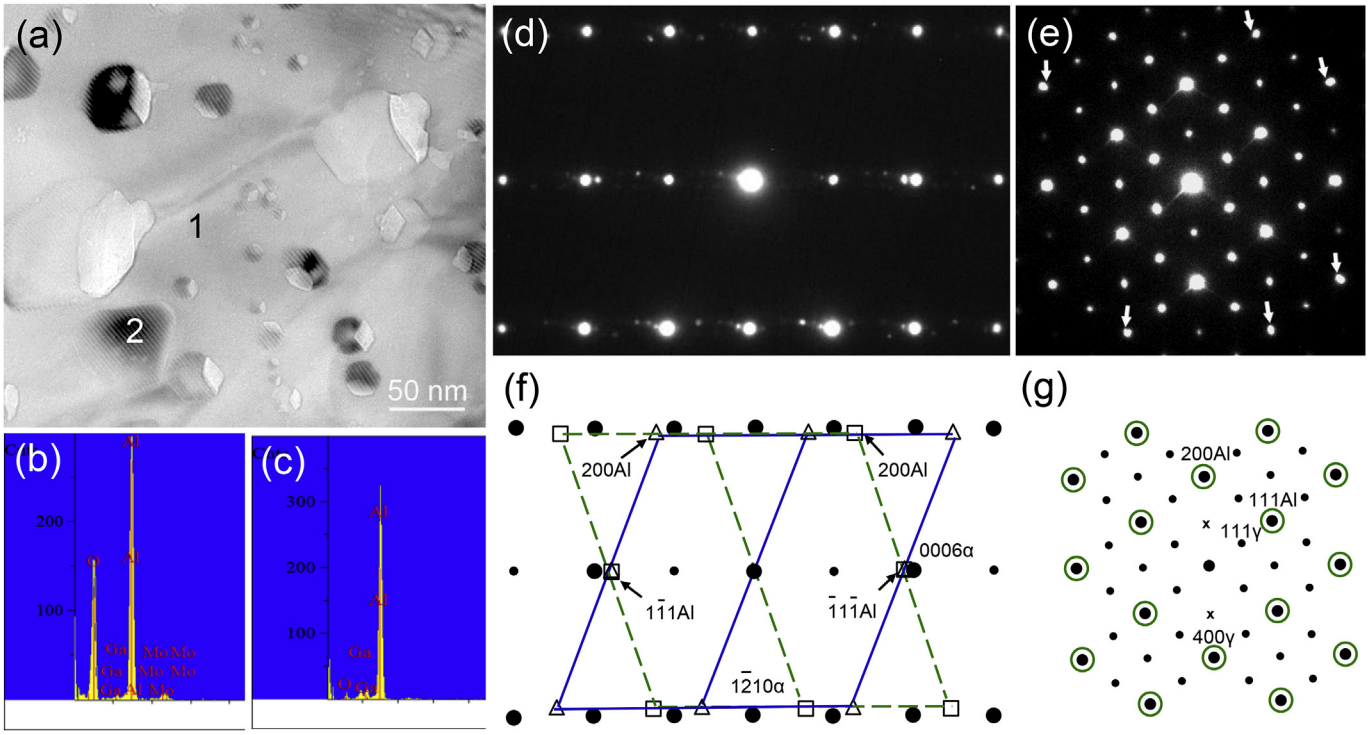

Fig. 9. (a) Nano precipitates in Al_2O_3 after plasma exposure for 3min; (b) and (c) EDS spectra of regions 1 and 2 in (a), respectively; (d) and (e) SAED patterns taken from α-Al_2O_3 and γ-Al_2O_3 regions containing the precipitates, respectively; (f) and (g) schematic SAED patterns of (d) and (e), respectively.

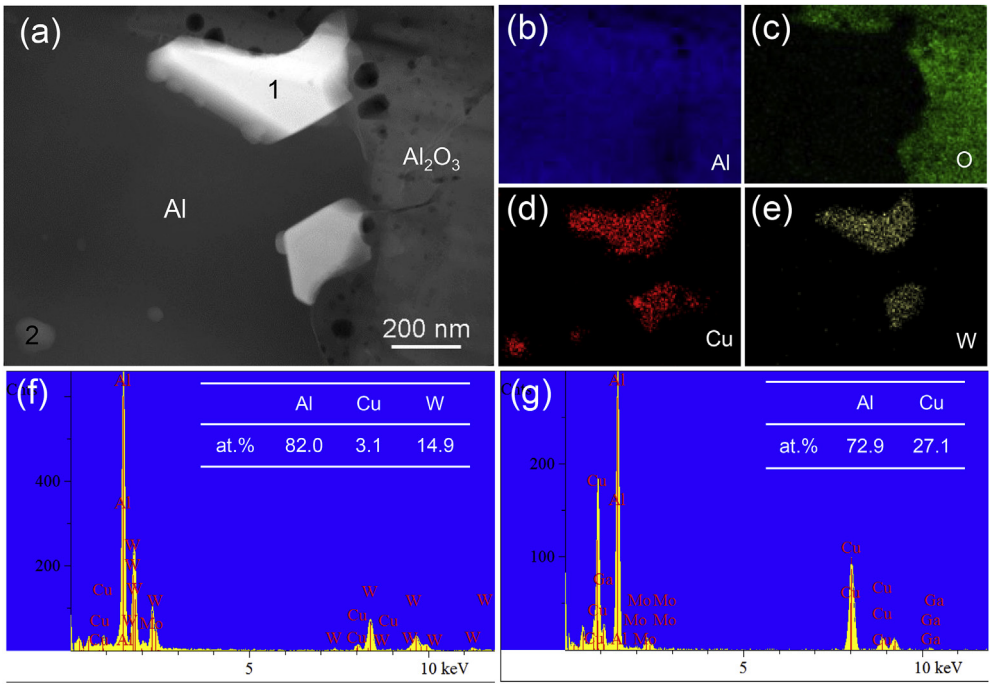

Fig. 10. HAADF-STEM image (a) and its EDS mappings (b)–(e) of Al/Al_2O_3 interface after plasma exposure for 3 min, (f) and (g) EDS spectra of regions 1 and 2, respectively.

Fig. 12(a) and (b) identified them to be tetragonal Al_2Cu. While the Al_2Cu nanoparticles were randomly oriented, the surface Al_2Cu dendrites developed an orientation relationship with Al as $(310)_{Al2Cu}//(010)_{Al}$ and $[001]_{Al2Cu}//[001]_{Al}$ (Fig. 12(c)), consistent with the relationship developed between Al and Al_2Cu in solidified Al-Cu alloy [22].

Diffraction patterns from the Al_5(W,Cu) particles did not match any known compound composed of Al, W and/or Cu. To determine the crystal lattice, a series of SAED patterns in several orientations were collected by large angle tilting, and the results are shown in Fig. 13. According to the geometric configuration of each pattern and the angles between any two patterns, a rhombohedral

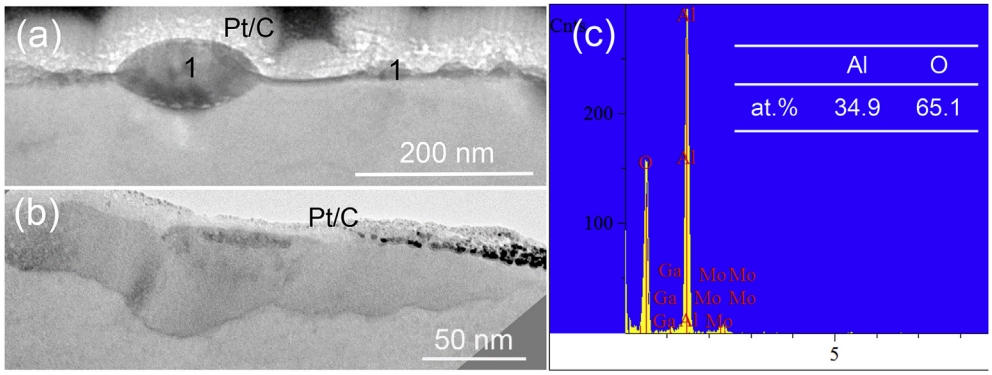

Fig. 11. TEM image of the surface nanostructures (a) and dendrites (b) developed in the Al region; (c) EDS spectra of region 1.

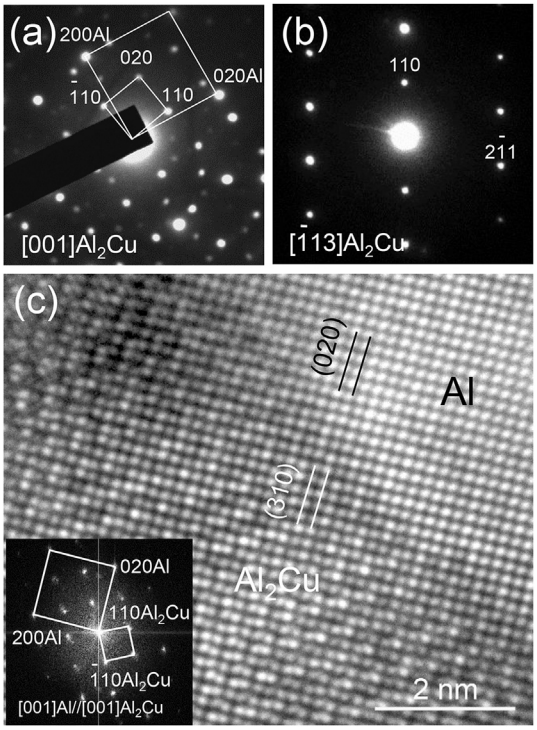

Fig. 12. NBD patterns of the Al_2Cu nanoparticles taken from: (a) [001] and (b) [−113] directions, respectively; (c) HRTEM of the interface between surface Al_2Cu dendrites and Al.

structure with lattice parameters $a = 0.490(3)$ nm, $c = 2.632(4)$ nm was deduced. The reflection conditions were shown in Table 1, suggesting the candidate space group to be $R3c$ or $R\bar{3}c$. To determine the crystal symmetry, convergent-beam electron diffraction (CBED) was used. Fig. 14 is a CBED pattern taken from the [0001] direction. The bright-field disc indicated $3m$ symmetry, while the zero-order Laue zone (ZOLZ) discs confirmed $6mm$ symmetry. The corresponding point group was then $\bar{3}m$, and the space group of $Al_5(W,Cu)$ was determined to be $R\bar{3}c$ [23].

Bright field TEM image of the $Al_5(W,Cu)$ particles revealed domain structure with domain size of ~3 nm, as seen in Fig. 15(a). HAADF-STEM image of Fig. 15(b) revealed that these domains were caused by the inhomogeneous distribution of heavy atoms. Such inhomogeneity was caused by a difference in Al/W atomic ratio, the brighter atomic columns were more W-rich than the darker ones, as evidenced by EDS spectra in Fig. 15(c) and (d). No arrangement difference was observed between different domains, and no additional weak reflections or diffuse intensity features were observed in the diffraction patterns.

4. Discussion

Under the exposure of high energy density plasma, Al_2O_3 experienced not only plasma and electrode bombardment, but also rapid heating and quenching that generated large temperature gradient from the surface to the bulk. As a result, besides surface erosion, substantial damage including formation of γ-Al_2O_3 on the surface, banded α-Al_2O_3 structures beneath the surface, cavities, Al precipitates and dislocations were generated down to a depth of ~1 μm. The simultaneous electrode impurities, especially W impurities, based on our experimental observations, accelerated the damage process by impurity sinking. Damage behavior on α-Al_2O_3 will be discussed from two aspects: plasma damage and impurity damage.

4.1. Plasma damage

Formation of metastable γ-Al_2O_3 on the surface of α-Al_2O_3 has been reported previously [21,24–26]. Three mechanisms have been proposed for the formation of γ-Al_2O_3: rapid solidification from the melt [24], annealing of the ion-irradiation induced amorphous Al_2O_3 below 1200 °C [27], and martensitic transformation from α-Al_2O_3 to γ-Al_2O_3 [25]. The irradiation-induced amorphization occurred at low temperature with high ion energy so as to create a high concentration of immobile defects [28]. The martensitic transformation was accompanied by twinning and interfacial dislocations [25]. In this study, the plasma ion energy was low, and twins or interfacial dislocations were not observed. It is therefore unlikely that γ-Al_2O_3 was formed by annealing of irradiation-induced amorphous Al_2O_3 or by martensitic transformation. Considering the high energy density of 20 J/cm^2 of the pulsed plasma, the surface γ-Al_2O_3 should be formed by rapid surface melting and quenching. The underneath α-Al_2O_3 banded regions (Figs. 5(a) and 7(d)) should then be the epitaxially related α-Al_2O_3 intergrowths grown from the plasma induced melt along the c direction. It is then reasonable to expect that due to surface melting, sinking of W particles was enabled.

It is interesting to note from Fig. 8 that even after plasma exposure for 30 min, thickness of the surface γ-Al_2O_3 layer caused by plasma is much smaller than that induced by 20 pulses laser with pulse duration of 40 ns (~200 nm) [24]. Besides surface melting and quenching that promoted formation of γ-Al_2O_3, the high energy density plasma also generated severe surface sputtering concurrently. As a combined result, thin γ-Al_2O_3 layer was

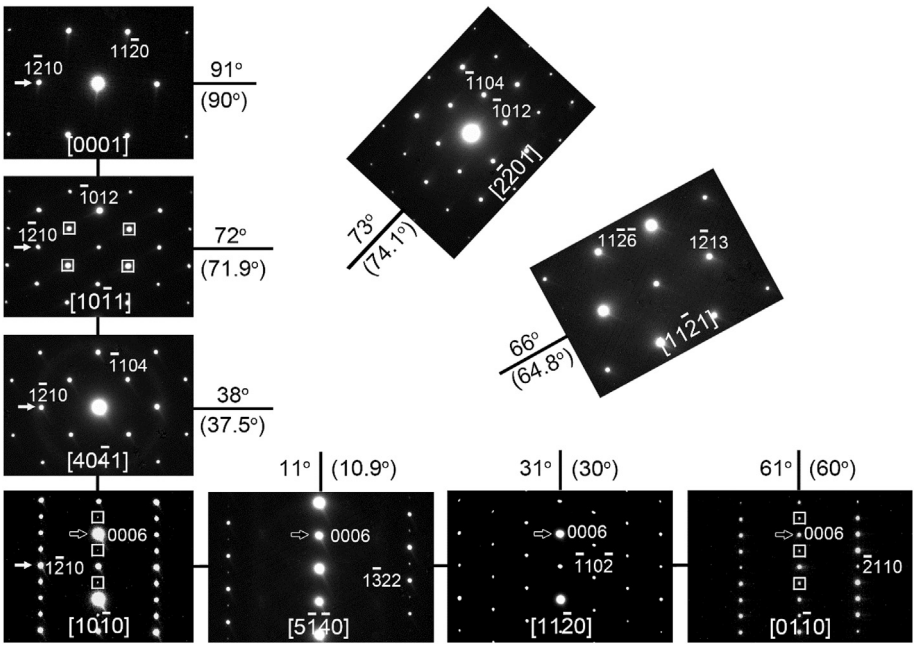

Fig. 13. A series of SAED patterns obtained from the Al_5(W,Cu) particle by large-angle tilting. The square-framed diffraction spots are resulted from double diffraction. The experimental angles (without parentheses) and calculated ones (within parentheses) are labeled.

Table 1
Reflection conditions of the Al_5(W,Cu) particle.

hkil	hki0	hh(−2h)l	h−h0l	000l	h−h00
$-h+k+l=3n$ or $l=2n$	$-h+k=3n$	$l=3n$	$h+l=3n$, $l=2n$	$l=6n$	$h=3n$

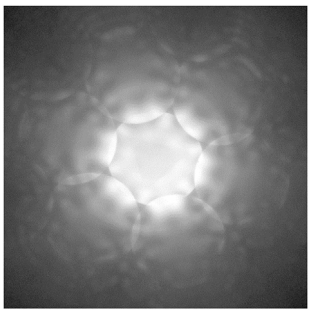

Fig. 14. CBED pattern of the Al_5(W,Cu) particle taken from [0001] direction.

developed on the plasma exposed surface. Thickness increase of the γ-Al_2O_3 layer with plasma exposure time should be caused by the decreased temperature gradient in α-Al_2O_3 due to its low thermal conductivity, which promoted development of larger γ-Al_2O_3 regions upon cooling.

Damage induced by plasma containing ions, electrons and photons can be caused mainly through knock-on damage and ionization. According to the Stopping and Range of Ions in Matter (SRIM) calculation, the maximum implantation depth of 14 keV Ar^+ ions into Al_2O_3 is ~15 nm. Such ion damage should have contributed mainly to the surface damage rather than to a depth of ~1 μm. For the energetic electrons, based on the conservation law of momentum for relativistic electrons, a minimum electron energy of ~175 keV is needed to initiate the knock-on damage on Al_2O_3 [29]. The electron energy in our plasma was far below the threshold necessary to achieve knock-on damage.

For the observed damage down to ~1 μm, the most likely cause was ionization that can induce damage deeper than that via knock-on process. This could be induced by both electrons and photons. The penetration depth of electrons in material can be approximated by: $x = 0.1\ E_0^{1.75}/\rho$, where, x is depth (μm), E_0 is electron energy (keV), and ρ is density (g/cm^3) [30]. Taking the density of α-Al_2O_3 as 4.0 g/cm^3, electron energy of above ~12 keV could cause damage down to 1 μm. For the z-pinch plasma with 2 kV discharge voltage, the energy of electrons could be accelerated to tens of keVs [31]. Such high energy electrons were able to cause a damage cross section of ~1 μm. On the other hand, the photons generated by plasma were in the extreme ultraviolet lithography (EUV) range with energy less than 124 eV. The photon penetration depth can be expressed as: $x = 1/\mu\rho$, where x is depth (cm), μ is mass absorption coefficient (cm^2/g), ρ is density (g/cm^3). For Al_2O_3, μ is around 10^5 cm^2/g at energy less than 124 eV [32], the photon penetration depth is then estimated to be ~25 nm, far less than 1 μm. It is thus confirmed that the deep damage was caused by electrons.

Based on the observed Al precipitates, electronic excitation-induced decomposition should be the main operative mechanism. A core-hole Auger decay mechanism has been proposed to explain the electronic excitation [33–35]. In this mechanism, the highest core level of Al (2p) is ionized by the incident electron and creates a hole. The created hole can be filled only by the inter-atomic Auger process because Al^{3+} has no free electrons. The transition of an electron from the 2p level of O^{2-} to the 2p level of Al^{3+} can be accompanied by an Auger yield of one or two electrons from the valence band. Having lost two or three electrons, the O^{2-} ion becomes a neutral O^0 or a positive O^+ ion and then desorbs to the surface or displaces to an interstitial site in the bulk due to Coulomb repulsion. This displacement caused vacancy-interstitial pairs in

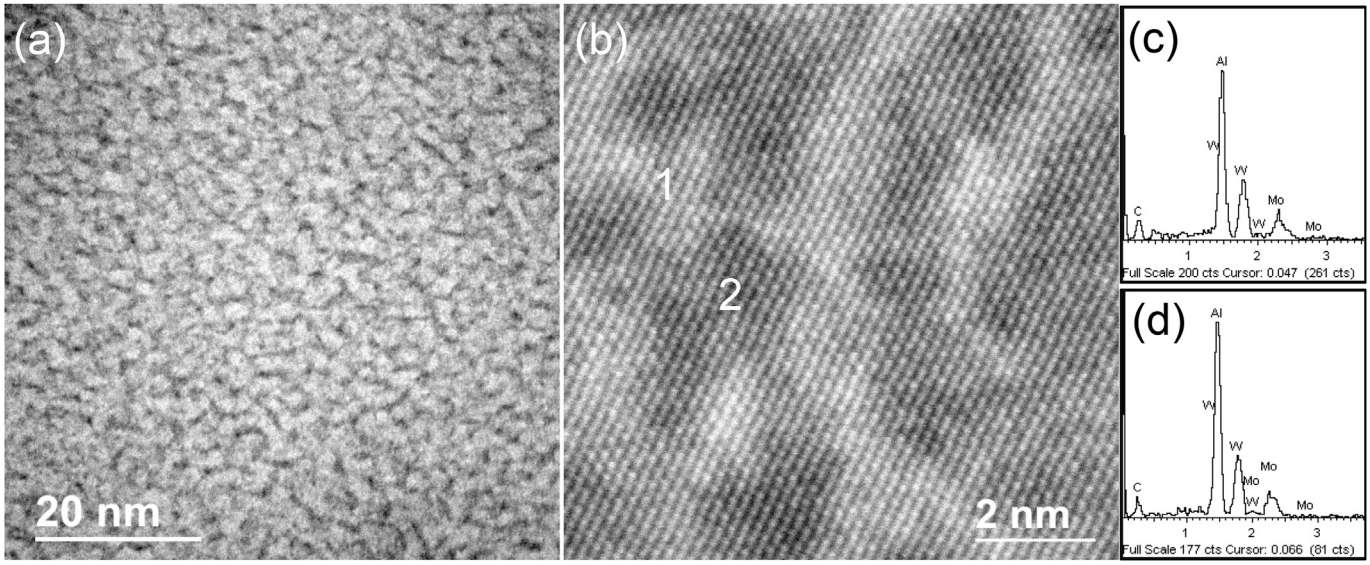

Fig. 15. (a) BF-TEM and (b) HAADF-STEM images of the Al_5(W,Cu) particle; (c) and (d) EDS spectra taken from regions 1 and 2 in (b), respectively.

the O sublattice. Once the Al cations are ionized down to a relatively deep-filled shell, Auger-induced decomposition occurs. At temperatures where the vacancies and interstitials in the O sublattice are mobile, aggregation of vacancies and interstitials would form Al colloids and O_2 bubbles, respectively [36]. An electron dose above 1×10^{19} cm^{-2} is needed for the decomposition of Al_2O_3 [37].

Under the bombardment of high density electrons (~10^{20} cm^{-3}) on a region of ~3 mm diameter, Al_2O_3 was able to decompose by electronic excitation at the beginning of plasma exposure. Evolution of the decomposed products with plasma exposure time should be caused by the combined influence of temperature and temperature gradient. At a shorter plasma exposure of 2 min, the temperature and temperature gradient in the bulk were low. Since the migration energy of an O interstitial is lower than that of an O vacancy (0.2–0.8 eV vs 1.8–2 eV) [14], O interstitials preferred to cluster into O_2 bubbles at low temperature, so that fine and uniform O_2 bubbles were formed (Fig. 5(a)). The observed cavities in plasma exposed samples should then be O_2 bubbles. As the exposure time increased to above 3 min, the increased electron fluence would increase the density of O defects. In addition, due to low thermal conductivity, the temperature experienced in Al_2O_3 should also increase. Both effects promote migration of not only O interstitials, but also O vacancies to form Al colloids and their coarsening. To minimize surface energy, the Al colloids were preferentially associated with O_2 bubbles (Fig. 9(a)). These Al colloids then crystallized as precipitates upon quenching, and developed orientation relationships with both α- and γ-Al_2O_3 to minimize the total free energy (Fig. 9). Similar orientation relationships between Al and α-Al_2O_3 have been reported in electron irradiated α-Al_2O_3 [38], while not yet between Al and γ-Al_2O_3. One should note that the largest Al precipitates and O_2 bubbles were located in the middle depth of the damage region, above which their size decreased (Fig. 7(a)). This is due to the bond loosening by extensive thermal vibration near the surface, so that O_2 desorption to the surface was enhanced. The thermally cracked grain boundaries, which acted as effective paths for O_2 desorption were then filled with the decomposed Al strips at increased exposure time (Figs. 3(a) and 7(a)). The underlying dislocations should be caused by the local stress generated by particle and bubble coarsening.

The surface nanostructures (Fig. 4(a)) that were not distinguishable by TEM, may be amorphous by the rapid quenching from the surface melt [18,19], or Al precipitates by O_2 desorption [39]. Furthermore, the Al_2O_3 nanoparticles on the surface of Al regions (Fig. 4(b)) should be from oxidation of Al with the desorbed O_2 from the bulk.

4.2. Electrode impurity damage

Based on the expanded γ-Al_2O_3 and Al regions adjacent to the sunken W impurities, the effect of impurities, predominantly W impurities, on damage acceleration of Al_2O_3, should behave as a local heat source.

At the initial stage of plasma exposure, the sunken W particles decreased the local cooling rate of the Al_2O_3 melt, causing local expansion of the γ-Al_2O_3 region (Fig. 6(a)). After plasma exposure for 3 min where Al colloids formed, the W particles accelerated local decomposition of Al_2O_3, causing interlinking and expansion of the liquid Al region (Fig. 7(a)). Interlinking of Al regions repelled the O_2 bubbles to the Al/Al_2O_3 interface and promoted bubble aggregation. Because of the lower density of Al than that of Al_2O_3, solidification of the Al region beneath the surface upon cooling generated surface extrusion and bursting, causing exposure of Al region to the surface. Development of the large Al region and Al strips located mainly at the grain boundaries would break the preferred orientation relationship with Al_2O_3. Thus, a preferred ⟨001⟩ solidification orientation with the surface driven by temperature gradient was developed (Fig. 7 (a) and (b)). Concurrently, the electrode impurities reacted with liquid Al to form Al_5(W,Cu) and Al_2Cu intermetallics.

The sputtering product of Cu existed in two forms: one as particles that formed Al_2Cu dendrites and nanoparticles due to sinking of Cu into liquid Al followed by rapid quenching; another as attached to W particles, which was evidenced by the distribution of Cu within W particles in the 2 min exposed sample and formation of Al_5(W,Cu) particles upon further plasma exposure.

For the new Al_5(W,Cu) particles, since the atomic concentration difference was on Al and W in the domain structure (Fig. 15(b)), and the concentration of Cu was low, it is probable that Cu was randomly distributed within the lattice. The Al_5(W,Cu) was probably formed by the Al-W reaction. In the W-Al system, dissolution of W particles in liquid Al at 750–850 °C for less than 30 min followed by rapid quenching result in the formation of hexagonal

Al_5W ($P6_3$, $a = 0.4902$ nm, $c = 0.8857$ nm) [40]. In this study, reaction of W with liquid Al followed by rapid quenching resulted in Al_5(W,Cu) with a chemical composition close to that of Al_5W, but with a rhombohedral structure. By comparing the two crystal structures, we can find that the rhombohedral Al_5(W,Cu) has almost the same a as that of Al_5W, but three times the c-axis of Al_5W. Similar crystal structure differences can be found in Al_5Mo polymorphs.

In the Al-Mo system, the Al_5Mo has three polymorphs [41]: (i) the high temperature hexagonal Al_5Mo (H, $P6_3$, $a = 0.4912$ nm, $c = 0.8860$ nm), formed above 700 °C; (ii) the low temperature rhombohedral Al_5Mo (R, $R\bar{3}c$, $a = 0.4951$ nm and $c = 2.623$ nm), formed below 650 °C, which is a stacking variant of Al_5Mo(H) with the c-axis three times that of Al_5Mo(h); and (iii) the intermediate temperature hexagonal Al_5Mo (H′, P_3, $a = 0.4933$ nm, $c = 4.398$ nm). The hexagonal Al_5Mo(H) is isotypic to Al_5W, and the Al_5Mo(R) is similar to our rhombohedral Al_5(W,Cu) with the same space group and close lattice parameters. Accordingly, the rhombohedral Al_5(W,Cu) observed in our study is probably a polymorph of Al_5W. Formation of the new Al_5(W,Cu) phase with Al- and W-rich nano domains may be caused by the introduction of Cu or plasma damage.

In the Al-W-Cu phase diagram, Cu is soluble in Al_5W at around 600 °C [42]. Since there is no Al-Cu-W phase diagram below 600 °C, one could not exclude the possibility that such a rhombohedral structure is a low temperature polymorph of Al_5W caused by the introduction of Cu. It has been reported that for both metals and oxides, the ultrafast electronic excitation together with high temperature could increase the electron density and dramatically alter interatomic forces. This in turn could induce structural transformation, such as nonthermal melting or phase transformation at very short time [43,44]. Under such conditions, the dynamically stable phase becomes unstable and transforms to a dynamically unstable phase. In our study, it is possible that the pulsed electronic excitation and high electron temperature could cause the formation of dynamically unstable rhombohedral Al_5(W,Cu) with nano domains, rather than the hexagonal structure. A complete Al-W-Cu phase diagram and further electron density and free energy calculations are needed to verify these hypotheses.

4.3. Summary of plasma damage on α-Al_2O_3

Based on the above discussion, one can deduce that besides plasma-induced surface erosion that can be caused by ions, electrons or even photons, decomposition within the bulk of Al_2O_3 also occurred by high density electrons. This bulk decomposition was substantially accelerated by the sunken electrode impurities. Such structural damage is destructive for ceramics used in a plasma thruster. Firstly, formation of Al alters the insulating nature and changes plasma equilibrium. Secondly, the overall sputtering rate of Al_2O_3 is severely accelerated by the formation of Al with a high sputtering rate. Therefore, besides surface erosion, potential electron damage in the bulk should also be considered for ceramics used in plasma thruster. To minimize electron damage in the bulk, three factors should be controlled. First, the electron density needs be controlled below a threshold dose for decomposition. Second, the electron energy needs to be low so as to reduce the ionization cross-section down to the knock-on cross-section caused by ions. Taking the present plasma condition on Al_2O_3 for example, the electron energy should be less than ~0.75 keV so as to reduce the ionization cross-section down to the ion implantation depth of ~15 nm. Third, the temperature experienced in the bulk needs to decrease in order to hinder defect aggregation. While the first two factors are controlled by the design of plasma source, the last factor can be controlled by eliminating electrode contamination, especially those having a high melting point. Further work on direct detection of plasma-induced defects, comprehensive microstructure damage on ceramics caused by plasma with different application conditions, and material design to increase plasma resistance are desired for enhancing material durability in plasma thruster.

5. Conclusions

1) High energy density plasma-induced damage on α-Al_2O_3 includes not only surface damage but also damage down to a depth of ~1 μm.
2) The surface damage includes surface nanostructures, grain boundary cracking, formation of surface γ-Al_2O_3, and epitaxial intergrowth of α-Al_2O_3 beneath the surface. Such damage is caused mainly by ion-based sputtering, and rapid surface melting and quenching.
3) The deep damage is characterized mainly by formation of Al nano precipitates and associated O_2 bubbles in both α- and γ-Al_2O_3. Such damage is proposed to be caused by the high density electron-induced decomposition of Al_2O_3 through electronic excitation. The decomposition is accelerated at increased exposure time and temperature. Crystallographic orientation relationships between the Al precipitates and Al_2O_3 have been determined as: $(111)_{Al}//(0001)_{\alpha\text{-}Al2O3}$, $[011]_{Al}//[10\bar{1}0]_{\alpha\text{-}Al2O3}$, and $(200)_{Al}//(400)_{\gamma\text{-}Al2O3}$, $[011]_{Al}//[011]_{\gamma\text{-}Al2O3}$.
4) The electrode impurities, especially W impurities, act as a local heat source by particle sinking, causing expansion of γ-Al_2O_3 and Al regions. The expanded Al region developed a $\langle 001\rangle_{Al}$ direction along the surface normal. Furthermore, the impurities reacted with Al to form Al_2Cu and Al_5(W,Cu) particles. The Al_2Cu were formed as surface dendrites and nanoparticles within the Al matrix. The Al_5(W,Cu) contained nano domains and was determined to be a rhombohedral structure having lattice parameters of $a = 0.490(3)$ nm, $c = 2.632(4)$ nm and a space group of $R\bar{3}c$.

Acknowledgement

The authors thank Prof. Jian-Min Zuo for valuable discussions on TEM imaging and analysis, and Patrick F. Keane for sample preparation. This work was supported by AFOSR Grant- 919 AF Sub TX UTA 11-000843 and AFOSR Grant FA9550-15-1-0107. The work was carried out in part in the Frederick-Seitz Materials Research Laboratory, Center for Microanalysis of Materials at the University of Illinois at Urbana-Champaign.

References

[1] D. Naujoks, Plasma-material Interaction in Controlled Fusion, Springer, 2006.
[2] G. Federici, C.H. Skinner, J.N. Brooks, J.P. Coad, C. Grisolia, A.A. Haasz, A. Hassanein, V. Philipps, C.S. Pitcher, J. Roth, W.R. Wampler, D.G. Whyte, Plasma-material interactions in current tokamaks and their implications for next step fusion reactors, Nucl. Fusion 41 (2001) 1967–2137.
[3] T. Burton, A.M. Schinder, G. Capuano, J.J. Rimoli, M.L.R. Walker, G.B. Thompson, Plasma-induced erosion on ceramic wall structures in Hall-effect thrusters, J. Propul Power 30 (2014) 690–695.
[4] Y. Garnier, V. Viel, J.F. Roussel, J. Bernard, Low-energy xenon ion sputtering of ceramics investigated for stationary plasma thrusters, J. Vac. Sci. Technol. A 17 (1999) 3246–3254.
[5] E. Ahedo, Plasmas for space propulsion, Plasma Phys. Contr. F. 53 (2011) 124037.
[6] R.L. Burton, P.J. Turchi, Pulsed plasma thruster, J. Propul Power 14 (1998) 716–735.
[7] D. Goebel, I. Katz, Fundamentals of Electric Propulsion Ion and Hall Thrusters, Wiley, New York, 2008.
[8] N. Gascon, M. Dudeck, S. Barral, Wall material effects in stationary plasma thrusters. I. parametric studies of an SPT-100, Phys. Plasmas 10 (2003) 4123–4136.
[9] V.V. Abashkin, O.A. Gorshkov, A.S. Lovtsov, A.A. Shagaida, Analysis of ceramic

erosion characteristic in Hall-effect thruster with higher specific impulse, in: International Electric Propulsion Conference. Florence,Italy, 2007, pp. 2007–2133.
[10] S.R. Gildea, T.S. Matlock, M. Martinez-Sanchez, W.A. Hargus, Erosion measurements in a low-power cusped-field plasma thruster, J. Propul Power 29 (2013) 906–918.
[11] X.M. Duan, D.C. Jia, Q.C. Meng, Z.H. Yang, Y. Yu, Y. Zhou, D.R. Yu, Y.J. Ding, Study on the plasma erosion resistance of ZrO_{2p}(3Y)/BN-SiO_2 composite ceramics, Compos. Part B 46 (2013) 130–134.
[12] W.J. Weber, R.C. Ewing, C.R.A. Catlow, T.D. de la Rubia, L.W. Hobbs, C. Kinoshita, H. Matzke, A.T. Motta, M. Nastasi, E.K.H. Salje, E.R. Vance, S.J. Zinkle, Radiation effects in crystalline ceramics for the immobilization of high-level nuclear waste and plutonium, J. Mater Res. 13 (1998) 1434–1484.
[13] M.I. Buckett, J. Strane, D.E. Luzzi, J.P. Zhang, B.W. Wessels, L.D. Marks, Electron-irradiation damage in oxides, Ultramicroscopy 29 (1989) 217–227.
[14] S.J. Zinkle, C. Kinoshita, Defect production in ceramics, J. Nucl. Mater 251 (1997) 200–217.
[15] P. Gessini, L.T.C. Habl, M.N.D. Barcelos Jr., J.L. Ferreira, M. Coletti, Low power ablative pulsed plasma thrusters, in: The 33 Rd International Electric Propulsion Conference, The George Washington University, USA, 2013.
[16] E.L. Antonsen, K.C. Thompson, M.R. Hendricks, D.A. Alman, B.E. Jurczyk, D.N. Ruzic, Ion debris characterization from a z-pinch extreme ultraviolet light source, J. Appl. Phys. 99 (2006) 063301.
[17] C. Rong, J.Z. Zhang, C.Z. Liu, S.Z. Yang, Surface metallization of alumina ceramics by pulsed high energy density plasma process, Appl. Surf. Sci. 200 (2002) 104–110.
[18] V. Surla, D. Ruzic, High-energy density beams and plasmas for micro- and nano-texturing of surfaces by rapid melting and solidification, J. Phys. D Appl. Phys. 44 (2011) 174026.
[19] R.S. Rawat, High-energy-density pinch plasma: a unique nonconventional tool for plasma nanotechnology, Ieee T Plasma Sci. 41 (2013) 701–715.
[20] D.T. Elg, J.R. Sporre, D. Curreli, I.A. Shchelkanov, D.N. Ruzic, K.R. Umstadter, Magnetic debris mitigation system for extreme ultraviolet sources, J. Micro Nanolithogr. MEMS MOEMS 14 (2015) 013506.
[21] I. Levin, D. Brandon, Metastable alumina polymorphs: crystal structures and transition sequences, J. Am. Ceram. Soc. 81 (1998) 1995–2012.
[22] W.W. Zhu, Z.M. Ren, W.L. Ren, Y.B. Zhong, K. Deng, Effects of high magnetic field on the unidirectionally solidified Al-Al_2Cu eutectic crystal orientations and the induced microstructures, Mater. Sci. Eng. A 441 (2006) 181–186.
[23] J.C.H. Spence, J.M. Zuo, Electron Microdiffraction, Plenum, New York, 1992.
[24] S.Q. Cao, A.J. Pedraza, D.H. Lowndes, L.F. Allard, γ-Al_2O_3 formation from pulsed-laser irradiated sapphire, Appl. Phys. Lett. 65 (1994) 2940–2942.
[25] P.F. Yan, K. Du, M.L. Sui, α- to γ-Al_2O_3 martensitic transformation induced by pulsed laser irradiation, Acta Mater 58 (2010) 3867–3876.
[26] P.S. Sklad, J.C. Mccallum, C.J. Mchargue, C.W. White, The amorphous-to-gamma transformation in ion-implanted Al_2O_3, Nucl. Instrum. Methods B 46 (1990) 102–106.
[27] C.W. White, L.A. Boatner, P.S. Sklad, C.J. Mchargue, J. Rankin, G.C. Farlow, M.J. Aziz, Ion-implantation and annealing of crystalline oxides and ceramic materials, Nucl. Instrum. Methods B 32 (1988) 11–22.
[28] W.J. Weber, Models and mechanisms of irradiation-induced amorphization in ceramics, Nucl. Instrum. Methods B 166 (2000) 98–106.
[29] G.P. Pells, D.C. Phillips, Radiation damage of α-Al_2O_3 in the HVEM: I. Temperature dependence of the displacement threshold, J. Nucl. Mater 80 (1979) 207–214.
[30] P.J. Potts, A Handbook of Silicate Rock Analysis, Chapman and Hall, New York, 1987.
[31] T. Zhang, J. Lin, A. Patran, D. Wong, S.M. Hassan, S. Mahmood, T. White, T.L. Tan, S.V. Springham, S. Lee, P. Lee, R.S. Rawat, Optimization of a plasma focus device as an electron beam source for thin film deposition, Plasma Sources Sci. T 16 (2007) 250–256.
[32] B.L. Henke, E.M. Gullikson, J.C. Davis, X-Ray Interactions - Photoabsorption, Scattering, Transmission, and Reflection at E=50-30,000 Ev, Z=1-92, At, 1993, pp. 181–342. Data Nucl. Data Tables 54.
[33] M.L. Knotek, P.J. Feibelman, Ion desorption by core-hole Auger decay, Phys. Rev. Lett. 40 (1978) 964–967.
[34] M.L. Knotek, P.J. Feibelman, Stability of ionically bonded surfaces in ionizing environments, Surf. Sci. 90 (1979) 78–90.
[35] S.D. Berger, I.G. Salisbury, R.H. Milne, D. Imeson, C.J. Humphreys, Electron energy-loss spectroscopy studies of nanometer-scale structures in alumina produced by intense electron-beam irradiation, Philos. Mag. B 55 (1987) 341–358.
[36] N. Itoh, K. Tanimura, Radiation effects in ionic solids, Radiat. Eff. Defect S 98 (1986) 269–287.
[37] A. Hoffman, P.J.K. Paterson, Electron stimulated reduction of sapphire studied by electron energy loss and Auger spectroscopies, Surf. Sci. 352 (1996) 993–997.
[38] T. Shikama, G.P. Pells, Radiation-damage in pure and helium-doped α-Al_2O_3 in the HVEM - qualitative aspects of void and aluminum colloid formation, Philos. Mag. A 47 (1983) 369–379.
[39] J.W. Park, A.J. Pedraza, W.R. Allen, Irradiation-induced decomposition of Al_2O_3 during Auger electron spectroscopy analysis, J. Vac. Sci. Technol. A 14 (1996) 286–292.
[40] Y.V.N.V.N. Yeremenko, V.I. Dybkov, Interaction of the refractory metals with liquid aluminium, J. Less Common Met. 50 (1976) 29–48.
[41] J.C. Schuster, H. Ipser, The Al-Al_8Mo_3 section of the binary-system aluminum-molybdenum, Metall. Trans. A 22 (1991) 1729–1736.
[42] http://mio.asminternational.org/apd/.
[43] P. Beaud, S.L. Johnson, E. Vorobeva, U. Staub, R.A. De Souza, C.J. Milne, Q.X. Jia, G. Ingold, Ultrafast structural phase transition driven by photoinduced melting of charge and orbital order, Phys. Rev. Lett. 103 (2009) 155702.
[44] Y. Giret, S.L. Daraszewicz, D.M. Duffy, A.L. Shluger, K. Tanimura, Nonthermal solid-to-solid phase transitions in tungsten, Phys. Rev. B 90 (2014) 094103.